Relevance of inter-particle interaction in directed energy deposition powder stream

Tijan Mede *, Matjaž Godec

The Institute of Metals and Technology, Lepi pot 11, Ljubljana, 1000, Slovenia

HIGHLIGHTS

- DED powder stream is shown to feature a large number of inter-granular collisions.
- Inter-granular collisions feature non-negligible rebound angles.
- Powder stream boundary condition has a key influence on grain collision statistics.

GRAPHICAL ABSTRACT
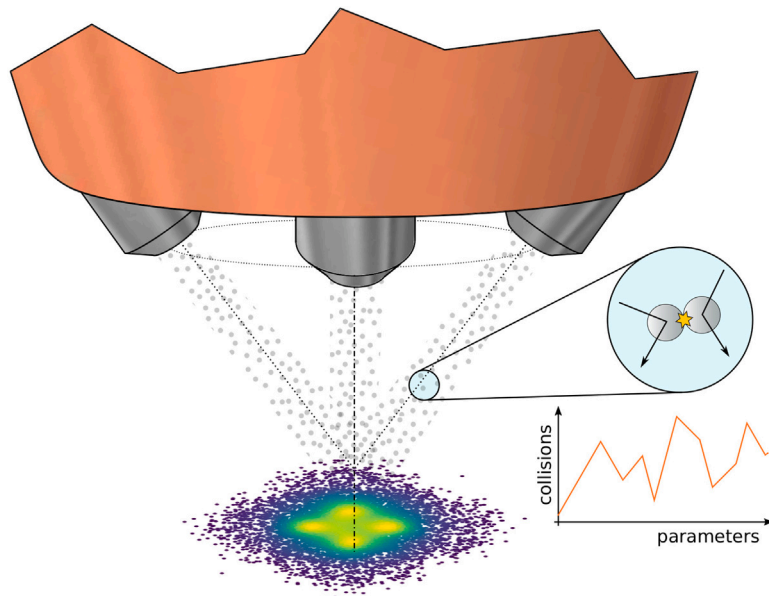
ABSTRACT

Blown powder dynamics is one of the aspects of Directed Energy Deposition (DED) with a major influence on deposition quality and potential for improvement in simulation. Most currently employed computational models discard powder grain collisions as negligible, although little explicit evidence for that claim exists. A Discrete Element Method approach is thus employed in the present work to simulate the actual number of grain collisions in a powder stream of a commercial discrete coaxial nozzle and how that number varies with the key processing parameters. While the number of powder grain collisions is found to in fact be negligible at one side of the usable parameter spectrum, the opposite side results in as many as 84% of all the powder grains being involved in inter-granular collisions with an average rebound angle of 14°, challenging the established hypothesis of the negligibility of this phenomena.

* Corresponding author.
  E-mail address: tijan.mede@imt.si (T. Mede).

1. Introduction

Metal-based additive manufacturing is potentially a disruptive technology across multiple fields [1], but likely holds the most significant potential for space and aviation industry [2,3]. Directed Energy Deposition (DED), in particular, is deemed highly appropriate for space applications due to the ability to operate in microgravity conditions, no imposed size limitation on the manufactured objects, and the ability to apply it to component repair [4]. These advantages however come at the expense of diminished dimensional accuracy, which at least partly originates from poor control and understanding of material deposition. The importance of the powder stream condition has been reported to have a major influence on the deposition quality and reproducibility of DED [5–7]. An accurate description of blow powder dynamics is thus considered a crucial ingredient of next-generation DED simulative models [8].

Analytical approaches have conventionally been employed to model the spatial distribution of particles exiting the nozzle and their interaction with the laser beam. Stream shape was typically approximated by idealized Gaussian distribution and particle trajectories by extrapolation of the nozzle passages [7,9,10], while Beer–Lambert law was employed to quantify attenuation of laser energy and powder temperature was calculated from particle exposure to the laser [9]. Modern analytical approaches are capable of accounting for variable particle velocity [11] and can compute powder distribution and temperature at the substrate level [12]. Due to high computational efficiency the analytical approaches are widely used by the manufacturers [13], but the models tend to rely on estimated experimental values for variables such as stream divergence [14].

Numerical approaches to modelling DED powder stream predominantly rely on computational fluid dynamics (CFD) to resolve a two-phase flow problem involving a dispersed second phase with the additional transport equation for the powder phase [15–18]. One-way coupling is applied, meaning that carrier gas is assumed to influence the trajectories of powder particles, but not vice-versa [15–18]. Powder particle dynamics are thus governed by the force balance between drag, gravity, and inertia while ignoring the inter-particle interactions. The use of numerical models allows for stream simulations without many of the assumptions usually adopted in the analytical approaches and has shown that assumptions such as straight powder particle trajectories and constant powder speed may not be warranted [14]. Interaction of powder particles with the nozzle walls was for instance shown to impose a governing effect on the particle trajectories, geometry of the powder jet, and particle density distribution [6,15,19,20]. Inelastic collisions with walls result in a velocity decrease after reflection, affecting the powder flow profile and focus [6]. Meanwhile, particle collisions are regularly neglected in numerical models of powder stream [6,15–18,21,22] on the account of occupying a relatively small volume fraction in the carrier gas flow [17]. The authors however offer little explicit evidence on the frequency of particle collisions and their influence on the powder stream. Moreover, a recently published numerical study [23] expanded this common approach by detecting particle collisions and resolving them using the Hertz theory, and reports a strong influence of the particle collisions on the powder particle dynamics in the case of a coaxial DED nozzle.

This paper aims to evaluate the relevance of inter-particle interactions on the powder stream in the example of a commercially available DED nozzle head. Discrete Element Method (DEM) [24] is applied as a state-of-the-art approach to mechanics of particle assemblies [25], capable of resolving inter-particle interactions. Stream of particles exiting a discrete coaxial DED nozzle head is simulated across a useful range of carrier gas volumetric fluxes, powder grain sizes, and deposition rates as defined by the nozzle head manufacturer while monitoring the grain collisions. As the focus of the study is evaluating the shear magnitude of inter-granular collision events rather than modelling the entire dynamics of the powder stream, the effects of the carrier gas, shielding gas, and surrounding atmosphere on the powder grain dynamics are neglected at this stage.
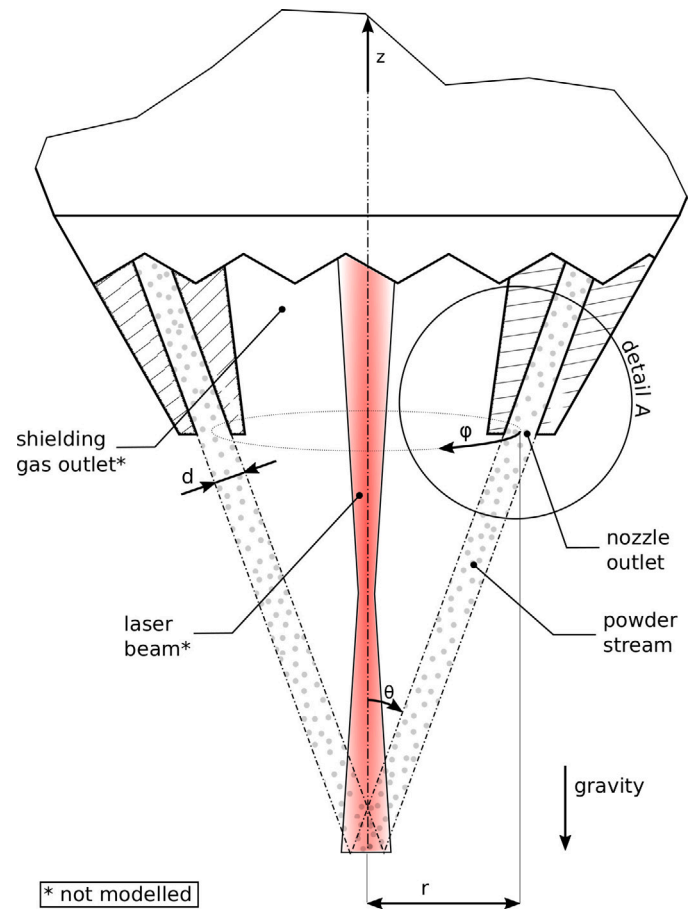

Fig. 1. Schematic representation of the Fraunhofer COAX 12V5 discrete coaxial nozzle model. Only two nozzle outlets (of the total four) can be observed in this cross-section.

Table 1
Key geometrical features of the Fraunhofer COAX 12V5 discrete coaxial nozzle and the utilized process parameters.

Parameter	Value
Number of nozzles	4
Radial nozzle displacement r [mm]	4.54
Nozzle outlet diameter d [mm]	1.5
Nozzle inclination angle θ [°]	19.25
Carrier gas volumetric flux ϕ_g [L/min]	2, 4, 6, 8
Powder particle radius r_p [µm]	15, 25, 35, 45, 55, 65, 75
Deposition rate $\dot{m}$ [g/min]	10, 15, 20, 25, 30, 35, 40, 45, 50

2. Numerical configuration

Open-source discrete element solver YADE [26] is utilized to model the stream of powder particles exiting a commercially available Fraunhofer COAX 12V5 discrete coaxial nozzle head and simulate particle trajectories within a pre-set domain. A schematic representation of the nozzle head is shown in Fig. 1, while key geometrical and process parameters are listed in Table 1. The substrate is not modelled in order to allow all the particle collisions to be followed, should no reflection from the substrate occur, decoupling the study of particle interaction from the variable stand-off distance. A cubical domain of 20 mm × 20 mm × 20 mm is considered, allowing grain collisions to be monitored separately within the minimal (13 mm) and maximal (20 mm) manufacturer-recommended stand-off distance from the nozzle. Powder particles are excluded from the simulation once they exit the domain. Simulations were performed for batches of 10 000 ideally spherical grains, where grains are generated at random locations at the nozzle
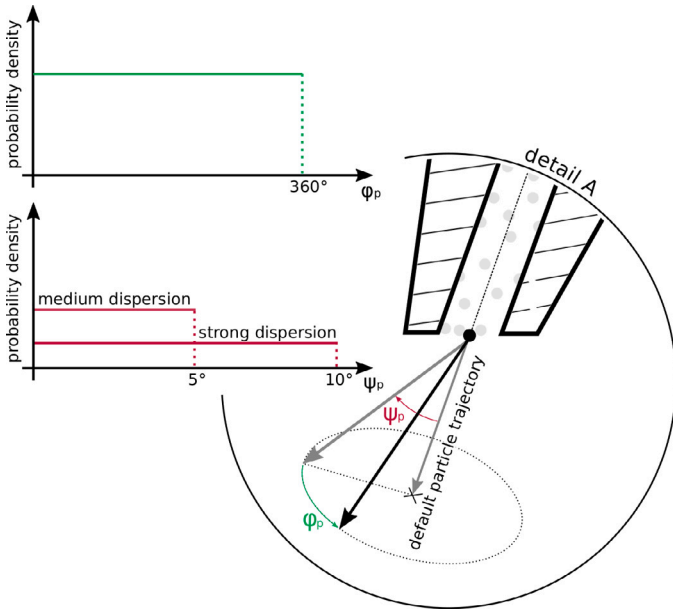
Fig. 2. Utilized probability distributions for the variation of the angles ψ_p and φ_p of the initial grain trajectories.
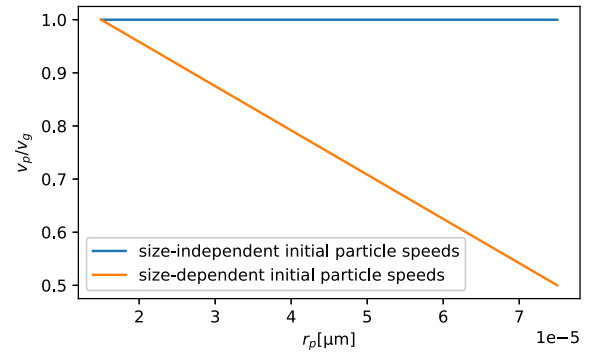

Fig. 3. Dependence of initial particle speed v_p with respect to carrier gas speed v_g plotted against particle radius r_p for the size-dependent and size-independent powder particle speed.

outlets (Fig. 2) and prescribed a uniform speed for each simulation run. Default initial grain trajectories are set parallel to the nozzle alignment, with optional random variations as detailed below. Gravitational force is applied parallel to the central axis of the DED head (Fig. 1) and zero Cundall's nonviscous damping is applied. Elastic grain collisions are resolved accounting for normal and frictional shear forces between ideally spherical powder particles according to the following contact laws [26]. Normal and shear contact stiffnesses are respectively defined as:

$$K_N = \frac{4E_1 r_1 E_2 r_2}{2E_1 r_1 + 2E_2 r_2} \tag{1}$$

$$K_S = \nu K_N, \tag{2}$$

where r_i and E_i are the radius and Young's modulus of the respective discrete particle and ν is the Poisson's ratio of the constituting material. Normal contact force F_N is defined with a linear dependence on the normal stiffness and penetration depth u_N:

$$F_N = K_N u_N, \tag{3}$$

while shear contact force F_S needs to be calculated as a sum of incremental shear forces:

$$\overline{F}_{S(i)} = \overline{F}_{S(i-1)} - K_S \Delta \overline{u}_{S(i)}, \tag{4}$$

where $\Delta \overline{u}_S$ is the incremental shear displacement. If the shear force exceeds the maximum shear force $F_{Smax} = \mu F_N$, where μ is the friction coefficient, a perfect plasticity is assumed:

$$\overline{F}_S = \overline{F}_{Smax} \frac{\overline{F}_S}{|\overline{F}_S|}. \tag{5}$$

The timestep Δt is set as a fraction (0.5) of the critical timestep Δt_{cr}, defined by insuring the elastic waves (travelling at the sonic speed of $\sqrt{E/\rho}$) do not propagate farther than the minimum distance between the integration points (diameter $2r_{min}$ of the smallest particle):

$$\Delta t = \frac{1}{2} \Delta t_{cr} = \frac{1}{2} 2r_{min} \sqrt{\frac{\rho}{E}} = r_{min} \sqrt{\frac{\rho}{E}}. \tag{6}$$

The powder particle radii r_p were considered uniform for each individual simulation run and deposition rate $\dot{m}$ and carrier gas flux

ϕ_g during individual simulations were kept constant. Separate simulations have been run for multiple values of powder particle size and deposition rate across the range recommended by the nozzle head manufacturer (Table 1). Carrier gas volumetric flux was varied within the typical range of values used with Fraunhofer coaxial nozzles [27, 28]. Particle speed v_p is derived from ϕ_g as detailed in the following paragraphs, assuming that the carrier gas velocity is uniform across the nozzle outlet. Physical properties of Inconel 718 as a typical material associated with DED were used for modelling the powder particles: Young's modulus $E = 208$ GPa, Poisson ratio $\nu = 0.294$, density $\rho = 8170$ kg/m^3, with friction coefficient estimated at $\mu = 0.3$ [29].

In order to simulate powder stream dispersion, initial grain trajectories are allowed to vary around the default trajectory which is set parallel to the central axis of each nozzle, by rotating the velocity vector first in the radial direction ψ_p and then in the azimuthal direction φ_p, as shown in Fig. 2. In accordance with the previously assumed [30–32] and measured [33] range of powder divergence angles for discrete DED nozzles, the utilized probability distributions for the random variations of the initial grain trajectories are as follows: *no dispersion* refers to no variation in the angle ψ_p of the initial grain trajectory; *medium dispersion* refers to homogeneous variation of ψ_p in the interval [0°, 5°]; *strong dispersion* refers to homogeneous variation of ψ_p in the interval [0°, 10°], while φ_p is allowed to vary homogeneously in the interval [0°, 360°].

Certain authors [6,17,21] indicated that powder particle speed at DED nozzle exit is dependent on the particle size as the larger particles lose momentum during consecutive collisions with the inner nozzle walls, while smaller particles with sufficiently low Stokes number follow the carrier gas streamlines and maintain speed [34]. These results however stem from numerical studies rather than measurements and have not been explored across a range of usable process parameters. A size-independent initial powder particle speed on the other hand continues to be utilized in state-of-the-art studies [7]. The effect of size-dependent as well as size-independent initial powder particle speeds on particle collision statistics is thus explored in this paper. In the case of size-independent initial particle speeds, the approach from [7] is adopted and the particle speeds are considered equal to the carrier gas speed at the nozzle outlet as shown in Fig. 3. In the case of size-dependent initial particle speeds, results from a numerical study on a similar discrete coaxial nozzle with nearly identical grain size distribution and carrier gas volumetric flux [17] are used to approximate the functional dependence of v_p/v_g on particle radius r_p, where, v_p is the initial particle speed and v_g is the carrier gas speed at the nozzle outlet. As depicted in Fig. 3, powder particles at $r_p = 15\,\mu$m are assigned a speed equal to that of the carrier gas and a linearly diminishing dependence on r_p is adopted, resulting in powder particles at initial speed half that of carrier gas at $r_p = 75\,\mu$m.
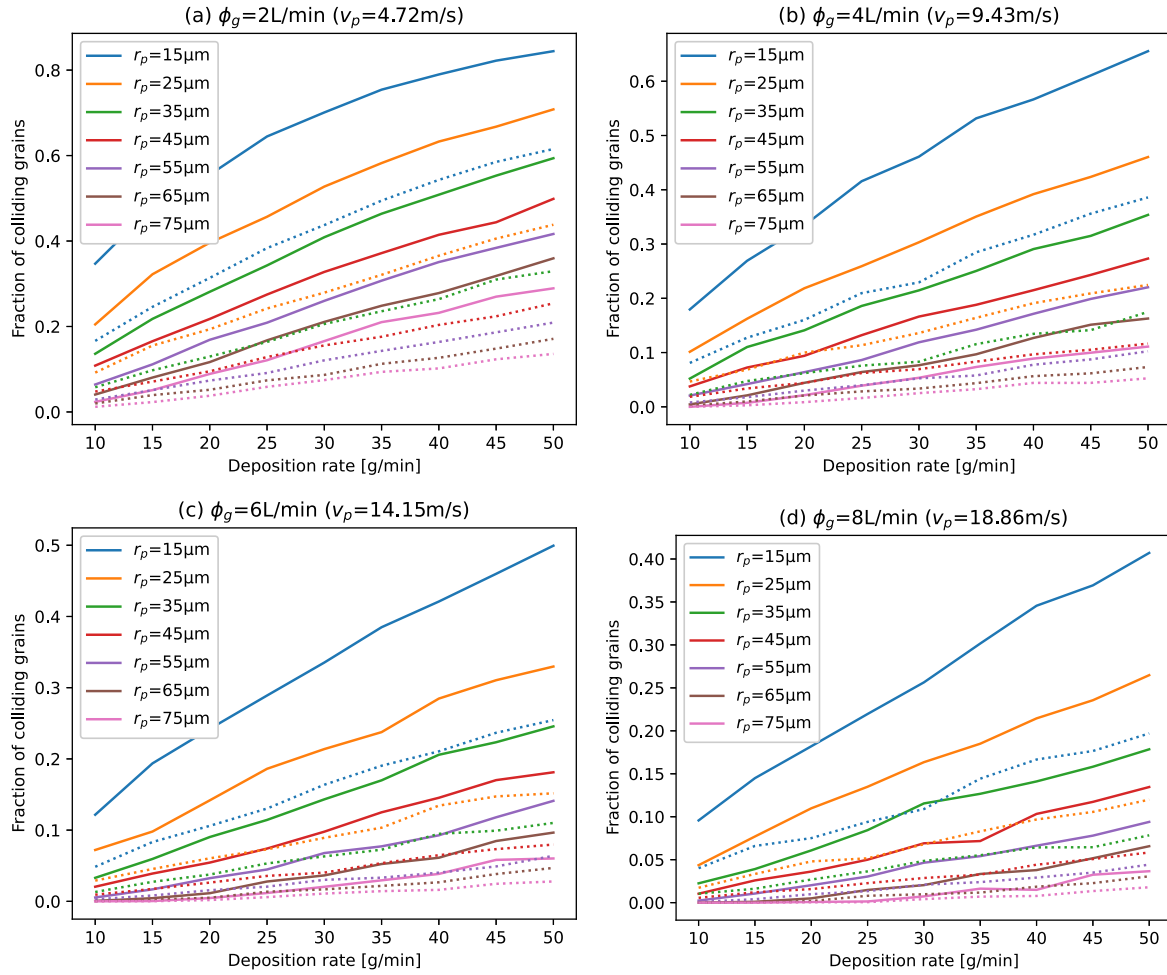
Fig. 4. Fraction of grains involved in inter-granular collisions at medium dispersion, size-independent initial particle speeds and carrier gas fluxes: $\phi_g = 2$ L/min (a), $\phi_g = 4$ L/min (b), $\phi_g = 6$ L/min (c) and $\phi_g = 8$ L/min (d). Solid and dotted lines represent collisions taking place within the maximal (20 mm) and minimal (13 mm) recommended stand-off distance from the nozzle respectively.
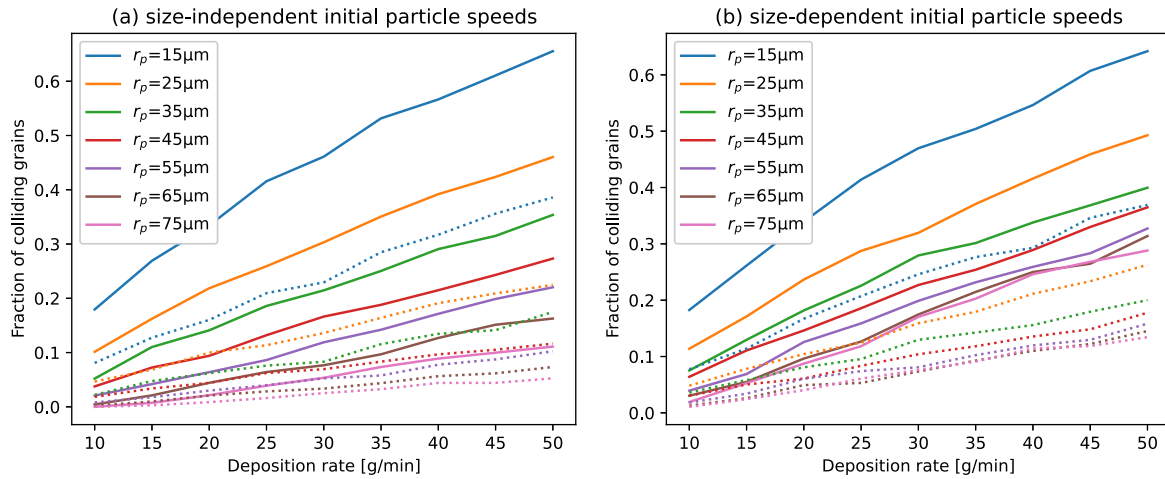
3. Results

The fraction of powder particles involved in inter-granular collisions in the simulation of powder stream from the studied nozzle is analysed in Fig. 4. Each of the four sub-figures showcases the simulated fraction of colliding grains as a function of deposition rate for different powder grain sizes at respective carrier gas volumetric fluxes $\phi_g = 2$ L/min (a), $\phi_g = 4$ L/min (b), $\phi_g = 6$ L/min (c), $\phi_g = 8$ L/min (d) (resulting in powder particle speeds $v_p = 4.72$ m/s (a), $v_p = 9.43$ m/s (b), $v_p = 14.15$ m/s (c), $v_p = 18.86$ m/s (d)), assuming medium dispersion ($\psi_p = 5°$) and size-independent initial particle speeds. The solid lines mark the grain collisions taking place within the maximal manufacturer-recommended stand-off distance (20 mm), while dotted lines mark the collisions taking place within the minimal manufacturer-recommended stand-off distance (13 mm).

At $\phi_g = 2$ L/min (Fig. 4a) for $r_p = 15$ μm, the fraction of colliding grains within the domain of the maximal recommended stand-off distance (20 mm) starts at 0.35 at $\dot{m} = 10$ g/min, exhibits a diminishing gradient with deposition rate and reaches a value of 0.84 at $\dot{m} = 50$ g/min. Increasing the grain radius gradually produces more linear curves and lower fractions of colliding grains. The largest tested grain radius $r_p = 75$ μm results in a 0.02 collision fraction at the lowest deposition rate and 0.28 collision fraction at the highest deposition rate. The dependency of the powder grain collision fraction on the grain size and

deposition rate within the domain of the minimal recommended stand-off distance (13 mm) exhibits a similar trend at lower absolute values. For the smallest simulated grain size $r_p = 15$ μm, a collision fraction of 0.17 is observed at $\dot{m} = 10$ g/min, and collision fraction of 0.62 is recorded at $\dot{m} = 50$ g/min. With increasing powder particle radius, the collision fraction curves become increasingly linear and exhibit lower values. For the largest simulated grain radius, a collision fraction of 0.01 is recorded at $\dot{m} = 10$ g/min, and a fraction of 0.14 is observed at $\dot{m} = 50$ g/min.

Increasing carrier gas volumetric flux to $\phi_g = 4$ L/min (Fig. 4b) produces somewhat less pronounced concave curves of grain collision fractions at smaller powder grain sizes. Within the domain of maximal recommended stand-off distance (20 mm) for the smallest grains with $r_p = 15$ μm, the simulated collision fraction is 0.17 at $\dot{m} = 10$ g/min and 0.66 at $\dot{m} = 50$ g/min. Gradually increasing the grain size steadily decreases the grain collision fractions, while the concave shape of curves is progressively replaced by more linear dependencies. For the largest simulated grain size of $r_p = 75$ μm, the lowest applied deposition rate results in zero powder particle impacts, while the highest deposition rate produces a collision fraction of 0.11. Looking at the minimal recommended stand-off distance (13 mm) a slightly concave grain collision curve is observed for the smallest grain size $r_p = 15$ μm, exhibiting a collision fraction of 0.08 at $\dot{m} = 10$ g/min and 0.39 at $\dot{m} = 50$ g/min. With increasing powder particle radius, the collision fraction

Fig. 5. Fraction of grains involved in inter-granular collisions at carrier gas volumetric flux $\phi_g = 4$ L/min and medium dispersion ($\psi_p = 5°$), applying size-independent (a) and size-dependent (b) initial particle speeds respectively. The solid lines represent the collisions taking place within the maximal recommended stand-off distance (20 mm) from the nozzle, while the dotted lines represent the collisions taking place within the minimal recommended stand-off distance (13 mm) from the nozzle.

curves become increasingly linear and exhibit lower values. At $r_p = 75\,\mu m$, no collisions are recorded for the lowest deposition rate and a collision fraction of 0.05 is observed at $\dot{m} = 50$ g/min.

Further increasing the gas volumetric flux to $\phi_g = 6$ L/min (Fig. 4c) additionally reduces the concave character of the grain collision fraction curves within the maximal recommended stand-off distance (20 mm) for the smallest powder particles in favour of a more linear shape. At $r_p = 15\,\mu m$ a collision fraction of 0.12 is observed for $\dot{m} = 10$ g/min and a collision fraction of 0.50 is recorded at $\dot{m} = 50$ g/min. Gradually increasing the grain size steadily decreases the grain collision fractions, while the concave shape of curves is progressively replaced by a slightly convex shape of the grain collision dependencies on deposition rate. For the lowest simulated grain radius $r_p = 75\,\mu m$, no impacts are observed for deposition rates $\dot{m} \leq 25$ g/min, and a collision fraction of 0.06 is recorded at $\dot{m} = 50$ g/min. Looking at the minimal recommended stand-off distance (13 mm), a roughly linear curve is observed for the smallest powder grain size $r_p = 15\,\mu m$, with collision fraction 0.05 at $\dot{m} = 10$ g/min and a collision fraction of 0.25 at $\dot{m} = 50$ g/min. With increasing grain radius, the grain collision curves progressively exhibit lower values but maintain a roughly linear shape. At $r_p = 75\,\mu m$, no collisions are recorded at the lower end of the deposition rate spectrum and a collision fraction of 0.03 is observed at $\dot{m} = 50$ g/min.

These trends are preserved when increasing the gas volumetric flux to $\phi_g = 8$ L/min (Fig. 4d). Observing powder particle collisions within the maximal recommended stand-off distance (20 mm), only a hint of concave shape is observed for the collision fraction curves at the smallest particle sizes. At $r_p = 15\,\mu m$ a collision fraction of 0.10 is observed for $\dot{m} = 10$ g/min and a collision fraction of 0.41 is recorded at $\dot{m} = 50$ g/min. Gradually increasing the grain size steadily decreases the grain collision fractions, while the concave shape of curves is progressively replaced by a slightly convex shape of the grain collision dependencies on deposition rate. For the largest grain radius $r_p = 75\,\mu m$, no collisions are observed for $\dot{m} \leq 20$ g/min, and a collision fraction of 0.04 is observed at $\dot{m} = 50$ g/min. Looking at the minimal recommended stand-off distance (13 mm), a roughly linear curve is observed for the smallest powder grain size $r_p = 15\,\mu m$, with collision fraction 0.04 at $\dot{m} = 10$ g/min and a collision fraction of 0.20 at $\dot{m} = 50$ g/min. With increasing grain radius, the grain collision curves progressively exhibit lower values but maintain a roughly linear shape. At $r_p = 75\,\mu m$, no collisions are recorded for $\dot{m} \leq 15$ g/min and a collision fraction of 0.02 is observed at $\dot{m} = 50$ g/min.

The influence of size-dependency of initial particle speeds on the powder grain collision frequency is analysed in Fig. 5. The two subfigures showcase the fractions of powder grains involved in intergranular collisions at carrier gas volumetric flux $\phi_g = 4$ L/min (resulting in carrier gas speed $v_g = 9.43$ m/s) and medium dispersion ($\psi_p = 5°$) for size-independent (a) and size-dependent (b) initial particle speeds respectively. In the former case the initial powder particle speed v_p is equal to that of the carrier gas v_g, while in the latter, the ratio of powder and carrier gas speed v_p/v_g is related to particle size as detailed in Fig. 3. The solid lines mark the grain collisions taking place within the maximal manufacturer-recommended stand-off distance (20 mm), while dotted lines mark the collisions taking place within the minimal manufacturer-recommended stand-off distance (13 mm).

In the case of size-independent initial particle speeds (Fig. 5a), concave curves of grain collision dependency on deposition rate can be observed for smaller grain sizes. Within the domain of maximal recommended stand-off distance (20 mm) for the smallest grains with $r_p = 15\,\mu m$, the simulated collision fraction is 0.17 at $\dot{m} = 10$ g/min and 0.66 at $\dot{m} = 50$ g/min. Gradually increasing the grain size steadily decreases the grain collision fractions, while the concave shape of curves is replaced by more linear dependencies. For the largest simulated grain size of $r_p = 75\,\mu m$, the lowest applied deposition rate results in zero powder particle impacts, while the highest deposition rate produces a collision fraction of 0.11. Within the domain of the minimal recommended stand-off distance (13 mm), a slightly concave grain collision curve is observed for the smallest grain size $r_p = 15\,\mu m$, exhibiting a collision fraction of 0.08 at $\dot{m} = 10$ g/min and 0.39 at $\dot{m} = 50$ g/min. With increasing powder particle radius, the concave shapes of curves are progressively replaced by more linear dependencies. At $r_p = 75\,\mu m$, no collisions are recorded for the lowest deposition rate and a collision fraction of 0.05 is observed at $\dot{m} = 50$ g/min.

Applying size-dependent initial particle speeds (Fig. 5b) and observing the domain of maximal recommended stand-off distance (20 mm) a collision fraction of 0.18 is observed at $\dot{m} = 10$ g/min and a collision fraction of 0.64 is recorded at $\dot{m} = 50$ g/min for the smallest powder particle radius $r_p = 15\,\mu m$ with a concave-shaped curve of collision fraction dependence on deposition rate. Gradually increasing the grain size steadily decreases the grain collision fractions, while the concave shape of curves is progressively replaced by more linear dependencies. For the largest powder grain size $r_p = 75\,\mu m$, a collision fraction of 0.02 is recorded at $\dot{m} = 10$ g/min and a collision fraction of 0.29 is observed at $\dot{m} = 50$ g/min. Within the domain of the minimal recommended

stand-off distance (13 mm), similar trends and collision curve shapes can be observed at lower values of collision fractions. At the smallest grain size $r_p = 15\,\mu m$, deposition rate of $\dot{m} = 10$ g/min results in a collision fraction of 0.08 and deposition rate of $\dot{m} = 50$ g/min results in a collision fraction of 0.37. For the largest grain size $r_p = 75\,\mu m$, deposition rate of $\dot{m} = 10$ g/min results in a collision fraction of 0.01 and deposition rate of $\dot{m} = 50$ g/min results in a collision fraction of 0.13.

The effect of boundary conditions at the nozzle outlet on inter-particle collision fractions is analysed in Fig. 6. The three sub-figures depict the fractions of powder grains involved in inter-granular collisions as functions of deposition rate and grain size at carrier gas volumetric flux $\phi_g = 4$ L/min (resulting in powder particle speed $v_p = 9.43$ m/s) and assuming size-independent initial powder particle speeds for three respective probability distributions for the variation of ψ_p in the initial grain trajectories. No variation in ψ_p is considered in Fig. 6a, while homogeneous probability distributions within ranges $[0°, 5°]$ and $[0°, 10°]$ are considered in Fig. 6b and c respectively. The solid lines mark the grain collisions taking place within the maximal manufacturer-recommended stand-off distance (20 mm), while dotted lines mark the collisions taking place within the minimal manufacturer-recommended stand-off distance (13 mm).

Applying no dispersion at the nozzle outlet (Fig. 6a) and observing the domain of the maximal recommended stand-off distance (20 mm) results in a fraction of colliding grains 0.28 at $\dot{m} = 10$ g/min and 0.82 at $\dot{m} = 50$ g/min with a concave curve in between for the smallest considered grain size $r_p = 15\,\mu m$. Gradually increasing the grain size steadily decreases the grain collision fractions, while the concave shape of curves is progressively replaced by a convex shape of the grain collision dependencies on deposition rate. For the largest grain radius $r_p = 75\,\mu m$ no collisions are recorded for $\dot{m} \leq 15$ g/min and a collision fraction of 0.18 is observed for $\dot{m} = 50$ g/min. Observing the domain of the minimal recommended stand-off distance (13 mm), similar trends and curve shapes are reproduced at lower absolute values of collision fractions. For the smallest studied grain radius $r_p = 15\,\mu m$ a collision fraction of 0.17 is observed at $\dot{m} = 10$ g/min and a collision fraction of 0.65 is recorded at $\dot{m} = 50$ g/min. With increasing grain radius, the grain collision curves progressively exhibit lower values and increasingly convex shape. At $r_p = 75\,\mu m$, no collisions are recorded for $\dot{m} \leq 15$ g/min and a collision fraction of 0.09 is observed at $\dot{m} = 50$ g/min.

Applying medium dispersion to the initial trajectories of powder particles (Fig. 6b) and observing the domain of the maximal recommended stand-off distance (20 mm) results in a fraction of colliding grains 0.17 at $\dot{m} = 10$ g/min and 0.66 at $\dot{m} = 50$ g/min with a slightly concave curve in between for the smallest considered grain size $r_p = 15\,\mu m$. Gradually increasing the grain size steadily decreases the grain collision fractions, while the concave shape of curves is progressively replaced by a quasi-linear shape of the grain collision dependencies on deposition rate. For the largest grain radius $r_p = 75\,\mu m$ no collisions are recorded at $\dot{m} = 10$ g/min and a collision fraction of 0.11 is marked for $\dot{m} = 50$ g/min. Observing the domain of the minimal recommended stand-off distance (13 mm), a slightly concave dependence of collision fractions on the deposition rate can be observed for $r_p = 15\,\mu m$ with collision fraction 0.08 at $\dot{m} = 10$ g/min and a collision fraction of 0.39 at $\dot{m} = 50$ g/min. With increasing grain radius, the grain collision curves become more linear and exhibit lower values. At $r_p = 75\,\mu m$, no collisions are recorded for $\dot{m} = 10$ g/min, and a collision fraction of 0.05 is observed at $\dot{m} = 50$ g/min.

Applying strong dispersion to the initial trajectories of powder particles (Fig. 6c) and observing the domain of the maximal recommended stand-off distance (20 mm) results in a fraction of colliding grains 0.13 at $\dot{m} = 10$ g/min and 0.50 at $\dot{m} = 50$ g/min with a slightly concave curve in between for the smallest considered grain size $r_p = 15\,\mu m$. Gradually increasing the grain size steadily decreases the grain collision fractions, while increasing the linear dependence of the grain collision
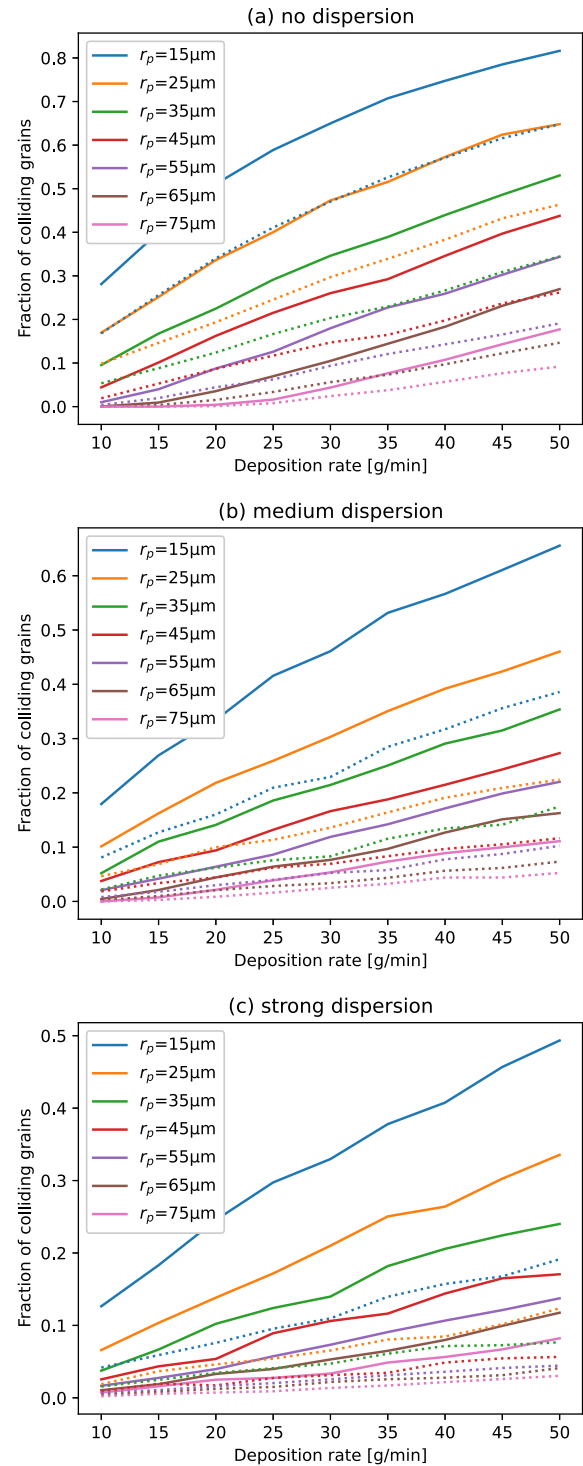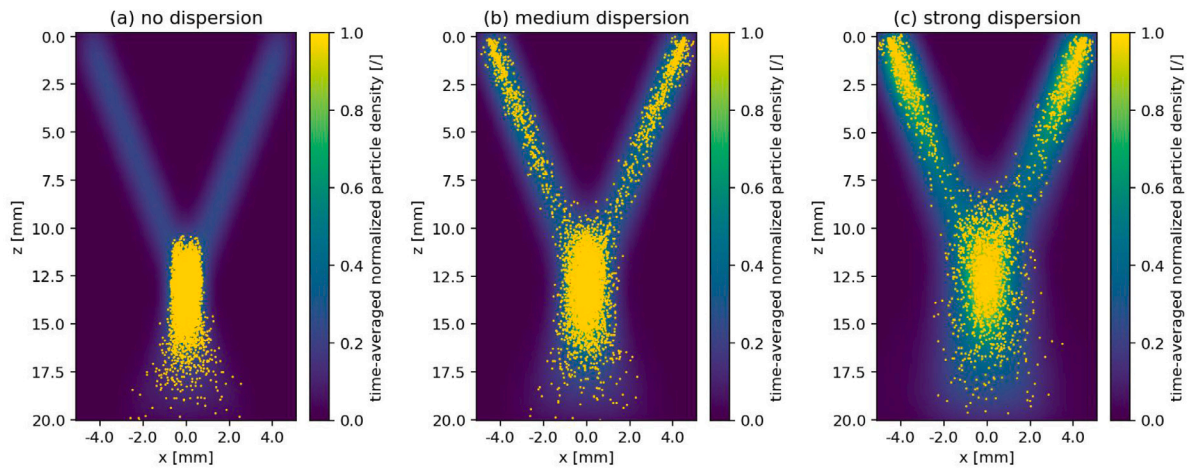

Fig. 6. Fraction of grains involved in inter-granular collisions at carrier gas volumetric flux $\phi_g = 4$ L/min and size-independent initial powder particle speeds, applying three different probability distributions for the variation the angle ψ_p of initial grain trajectories: no dispersion (a), medium dispersion (b), strong dispersion (c). The solid lines represent the collisions taking place within the maximal recommended stand-off distance (20 mm) from the nozzle, while the dotted lines represent the collisions taking place within the minimal recommended stand-off distance (13 mm) from the nozzle.

Fig. 7. Relative density plots of the simulated nozzle powder stream for carrier gas volumetric flux ϕ_g = 4 L/min, deposition rate $\dot{m}$ = 50 g/min, size-independent initial powder particle speeds and powder particle radius r_p = 15 μm, applying three different probability distributions for the variation of angle ψ_p of the initial grain trajectories: no dispersion (a), medium dispersion (b), strong dispersion (c). Averaged particle density across a thin x-z cross-section is plotted in the purple–yellow colour scale. Yellow dots represent locations of inter-granular collisions.

fractions on deposition rate. For the largest grain radius r_p = 75 μm, a 0.01 collision fraction is recorded at $\dot{m}$ = 10 g/min, and a collision fraction of 0.08 is observed for $\dot{m}$ = 50 g/min. Observing the domain of the minimal recommended stand-off distance (13 mm), a roughly linear dependence of collision fractions on the deposition rate can be observed for r_p = 15 μm with collision fraction 0.04 at $\dot{m}$ = 10 g/min and a collision fraction of 0.20 at $\dot{m}$ = 50 g/min. With increasing grain radius, the grain collision curves progressively exhibit lower values but maintain a roughly linear shape. At r_p = 75 μm, a 0.002 collision fraction is recorded at $\dot{m}$ = 10 g/min, and a collision fraction of 0.03 is observed at $\dot{m}$ = 50 g/min.

Analysis of inter-granular collision locations was performed for the simulated powder stream, applying carrier gas volumetric flux ϕ_g = 4 L/min (resulting in powder particle speed v_p = 9.43 m/s), deposition rate $\dot{m}$ = 50 g/min, size-independent initial powder particle speeds and powder particle radius r_p = 15 μm. The three sub-figures of Fig. 7 depict locations of inter-granular collision locations (yellow dots) against a background plot of time-averaged normalized 2D particle density plot of a thin 0.8 mm cross-section in x-z plane using three different probability distributions for the variation of the angle ψ_p of the initial grain trajectories: no dispersion (a), medium dispersion (b), strong dispersion (c). The relative particle density was evaluated by applying Gaussian kernel density estimation with Scott's Rule bandwidth estimation and subsequent Gouraud shading and normalization of values.

Observing the time-averaged powder particle density for the no-dispersion scenario in Fig. 7a, two non-diverging particle streams are visible, starting at the nozzle outlets in the two upper corners, crossing at (0 mm, 13 mm) and exiting the domain at (−2 mm, 20 mm) and (2 mm, 20 mm) respectively. The time-averaged particle density appears homogeneous along the particle streams with the exception of the intersection zone, where the density is strongly increased (although mostly concealed on the image by the collision locations). None of the inter-granular collisions appear above the intersection of the two powder streams, with a vast majority being concentrated within the domain of the intersection and a smaller number of instances appearing below the intersection domain.

The two averaged powder stream cross-sections are somewhat wider and diverging in the case of medium dispersion in Fig. 7b. Time-averaged particle density progressively diminishes with the distance from the nozzle outlets. The stream intersection can be observed to take up a larger area compared to the no-dispersion scenario. Particle collisions are somewhat more scattered around the stream intersection

and moreover appear also in both streams upward of the stream intersection, with lower density which however increases towards the nozzle outlets. A smaller number of grain collisions can also be observed below the stream intersection zone.

The two powder streams further widen and diverge in the case of strong dispersion in Fig. 7c, producing a continuous highly dispersed flux at the bottom of the domain. The reduction of the time-averaged particle density with the distance from the nozzle outlets is substantially more pronounced, resulting in concentration zones close to the nozzle outlets with a comparable particle density to the stream intersection zone, which in this case is further inflated. Grain collision concentration in the stream intersection zone is present but less pronounced and far more dispersed compared to Fig. 7a. and b. Similarly as in Fig. 7b, collision locations appear along the two powder streams upward of the stream intersection, with a notable increase in density in the zone of high time-averaged particle density close to the nozzle outlets. A non-negligible number of grain collisions also take place below the stream intersection.

In order to assess the magnitude of the effect that powder particle collisions have on grain trajectories, rebound angles in particle collisions were analysed (Fig. 8) for carrier gas volumetric flux ϕ_g = 4 L/min, deposition rate $\dot{m}$ = 50 g/min, size-independent initial powder particle speeds and powder particle radius r_p = 15 μm, applying three different probability distributions for the variation of angle ψ_p of the initial grain trajectories: no dispersion (a), medium dispersion (b), strong dispersion (c). For each collision, particle velocity vectors of the two colliding particles directly prior to the collision were compared with the post-collision velocity vectors to recover the rebound angles of both particles. Probability density functions (PDF) of collision rebound angles were then obtained by performing Gaussian kernel density estimation with Scott's Rule bandwidth estimation.

No initial dispersion PDF exhibits a sharp rise between 0° and 9°, a relatively slow quasi-linear decay between 9° and 25° and accelerated decay between 25° and 50° rebound angles. Medium dispersion PDF features a narrow peak at 3°, followed by a relatively constant plateau between 10° and 25° and a gradual decay between 25° and 50° rebound angles. Strong dispersion PDF exhibits a somewhat wider peak at 5°, followed by a quasi-constant plateau between 15° and 27° and a gradual decay between 27° and 50° rebound angles. Mean rebound angles for the no dispersion, medium dispersion, and strong dispersion scenarios are 15.2°, 13.8°, and 13.5° respectively.
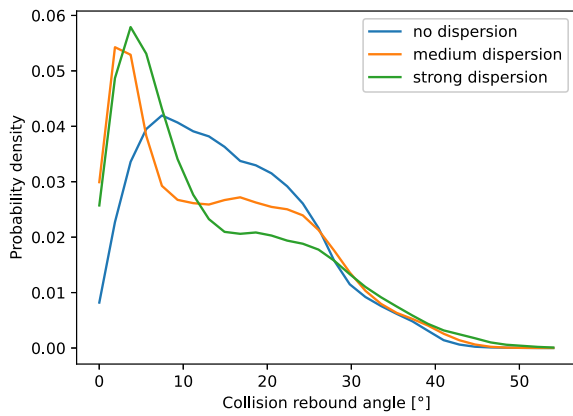
Fig. 8. Probability density functions of particle collision rebound angles in the simulated powder stream for carrier gas volumetric flux ϕ_g = 4 L/min, deposition rate $\dot{m}$ = 50 g/min, size-independent initial powder particle speeds and powder particle radius r_p = 15 µm, applying three different probability distributions for the variation of angle ψ_p of the initial grain trajectories: no dispersion (a), medium dispersion (b), strong dispersion (c).

4. Discussion

DEM simulations performed in this study offer a unique insight into the relevance of inter-particle interaction on dynamics of DED powder stream for the case of a widely used modern commercial discrete coaxial nozzle head. It should be emphasized again that the utilized model does not attempt to simulate the complexity of DED powder particle dynamics, but rather offers a crude estimation of the powder particle collision impact on the dynamics of the DED powder stream and should be interpreted as such. Although the utilized model does not account for the interaction between carrier gas and powder particles, the shear statistics of powder particle collisions can be expected to yield sensible results, providing that the particle density distribution along the powder stream is accurate. The utilized dispersion angles cover the range of previously assumed or measured values for powder stream divergence of discrete coaxial nozzles [30–33]. Powder particle density distribution can also be expected to be influenced by powder grain speed and its possible dependence on particle size. As the effect of initial powder particle speed dependence on its size is mostly based on results of numerical studies rather than experiments and since it has not been analysed over a range of relevant process parameter values, the size-dependence of powder particle speed is not adopted as a general initial condition in the present study, but rather explored in a separate sensitivity analysis, utilizing the published size dependency of particle speed for that particular set of process parameter values [17]. In the absence of more reliable data, the range of results presented in this paper can thus be expected to cover the range of possible powder stream density distributions relevant to this investigation. Nevertheless, due to the limitations of the utilized methodology, the simulation results analysis was limited to grain collision statistics, rather than powder particle density distribution at domain boundary, as altered trajectories of rebounded grains might be heavily influenced by the carrier gas.

The number of inter-granular collisions in the powder stream heavily depends on the utilized processing parameters, as can be observed in Fig. 4. Deposition rate has a positive effect on the number of collisions whereas carrier gas flux, grain size, and dispersion of particle trajectories all have a negative effect on the number of collisions. While inter-granular collision count approaches zero at the low deposition rate/large powder grains/high carrier gas flux/small stand-off distance side of the useful parameter spectrum, the opposite side of the spectrum features as many as 84% of all the powder grains being involved in collisions with other grains. Since the mean rebound angle for the

simulated scenarios is shown to be roughly 14° nearly independently of the applied parameters (Fig. 8), significant changes in the powder stream density distribution might occur as a result of inter-granular collisions across a large portion of the process parameter window.

Applying size-dependent initial particle speeds appears to maintain the trends observed when utilizing size-independent initial particle speeds (Fig. 5). Deposition rate has a positive effect on the number of collisions whereas grain size has a negative effect on the number of collisions. The absolute values of inter-granular collision fractions however increase due to the slower-moving larger powder grains, which is consistent with the higher collision fractions observed for lower powder particle speeds in Fig. 4. The effect of increased particle collision fractions, which is very pronounced for smaller particle sizes progressively decays with grain size. This corresponds to the utilized function relating particle speed to its size (Fig. 3), which applies a speed correction (with respect to the carrier gas speed) proportional to the grain size. While the functional dependence of initial particle speed to its size is unknown for other utilized combinations of process parameters and was thus not studied, it is important to note that diminished speeds of larger grains can only increase the observed collision fractions and thus further underline their importance.

The dispersion of initial grain trajectories is shown to have a considerable effect on the fraction of colliding powder particles and underlines the need to investigate the powder boundary conditions at the nozzle outlet. As underlined by Kovalev et al. [6], the carrier gas velocity, concentration, and inertial properties of powder particles, channel geometry, irregularities on powder particles, and wall roughness, as well as mechanical properties of powder and nozzle, can be expected to have an influence over particle–wall collisions and consequently particle trajectory dispersion at the nozzle outlet. This investigation suggests that the fraction of colliding grains decreases when larger dispersions of initial powder grain trajectories are allowed, but can still achieve up to 50% at the high deposition rate/small powder grains/large stand-off distance side of the useful parameter spectrum even when the largest considered dispersion is applied at a relatively conservative carrier gas flux. It should also be underlined that increased dispersion in initial grain trajectories also increases the fraction of inter-granular collisions that take place upstream of the stream intersection zone (Fig. 7). The increased distance between the collision location and the lower end of the domain can be expected to increase the displacement of particles (with respect to undisturbed particle trajectory) when entering the melt-pool/interacting with substrate. Although the boundary conditions at the nozzle outlet have not been experimentally analysed, the simulations have been performed across the range of expected powder stream dispersions and the results suggest that the powder grain collision fraction appears non-negligible for a large part of the process parameter window.

5. Conclusions and perspectives

A DEM-based numerical model has been applied to simulate granular dynamics of DED powder stream of a commercial discrete coaxial nozzle. The fraction of powder grains involved in inter-granular collisions has been analysed over a broad spectrum of usable process parameters. The fraction of colliding grains was found to vary considerably with the processing parameters and while a combination of low feeding rate, large powder grains, high carrier gas flux, and high dispersion of particle trajectories were found to produce a negligible number of inter-granular collisions, as many as 84% of powder grains were found to be involved in inter-granular collisions at the opposite side of the parameter spectrum. Furthermore, the mean powder particle collision rebound angles for the performed simulations were found to be approximately 14° nearly independently of the applied dispersion angle, suggesting marked alterations of grain trajectories during collisions. Accounting for the energy losses of larger particles due to consecutive collisions with the inner wall of the nozzle

through a size-dependent initial particle speed appears to maintain the observed trends in inter-granular collision fractions and moreover further increases the collision fractions, which additionally underlines the importance of this phenomena.

While the numerical simulations in this paper only investigate the powder grain collision statistics for the case of one particular example of a discrete coaxial DED nozzle and associated process parameters, the nozzle geometry and parameter ranges are comparable to a number of existing DED nozzles [10,17,22]. In summation, the conducted numerical campaign implies that the broadly accepted approach of ignoring inter-particle collisions in the DED powder stream [15–18] might not be warranted. The results of this study are also in line with the recent findings of Chai et al. [23] for the case of a continuous coaxial DED nozzle and underline the need to account for inter-particle collisions in future modelling of the blown powder dynamics of DED in order to achieve a high level of accuracy. A detailed analysis of the powder boundary condition at the nozzle will also be necessary to achieve this goal, as dispersion of initial grain trajectories was shown to have a critical effect on the dynamics of the DED powder stream.

CRediT authorship contribution statement

Tijan Mede: Writing – review & editing, Writing – original draft, Software, Methodology, Investigation, Formal analysis, Conceptualization. **Matjaž Godec:** Supervision.

Declaration of competing interest

The authors declare that they have no known competing financial interests or personal relationships that could have appeared to influence the work reported in this paper.

Data availability

No data was used for the research described in the article.

Acknowledgements

References

[1] J.H. Martin, B.D. Yahata, J.M. Hundley, J.A. Mayer, T.A. Schaedler, T.M. Pollock, 3D printing of high-strength aluminium alloys, Nature 549 (7672) (2017) 365–369.

[2] T.D. Ngo, A. Kashani, G. Imbalzano, K.T. Nguyen, D. Hui, Additive manufacturing (3d printing): A review of materials, methods, applications and challenges, Composites B 143 (2018) 172–196.

[3] S.M.A. Noori Rahim Abadi, P. Hagqvist, F. Sikström, I. Choquet, Cfd-based feasibility study of laser-directed energy deposition with a metal wire for on-orbit manufacturing, Front. Space Technol. 3 (2022) 880012.

[4] N. Shamsaei, A. Yadollahi, L. Bian, S.M. Thompson, An overview of direct laser deposition for additive manufacturing; part ii: Mechanical behavior, process parameter optimization and control, Addit. Manuf. 8 (2015) 12–35.

[5] S. Wen, Y. Shin, J. Murthy, P. Sojka, Modeling of coaxial powder flow for the laser direct deposition process, Int. J. Heat Mass Transfer 52 (25–26) (2009) 5867–5877.

[6] O. Kovalev, I. Kovaleva, I.Y. Smurov, Numerical investigation of gas-disperse jet flows created by coaxial nozzles during the laser direct material deposition, J. Mater Process. Technol. 249 (2017) 118–127.

[7] Z. Liu, H.-C. Zhang, S. Peng, H. Kim, D. Du, W. Cong, Analytical modeling and experimental validation of powder stream distribution during direct energy deposition, Addit. Manuf. 30 (2019) 100848.

[8] S.M. Thompson, L. Bian, N. Shamsaei, A. Yadollahi, An overview of direct laser deposition for additive manufacturing; part I: Transport phenomena, modeling and diagnostics, Addit. Manuf. 8 (2015) 36–62.

[9] Y.-L. Huang, J. Liu, N.-H. Ma, J.-G. Li, Three-dimensional analytical model on laser-powder interaction during laser cladding, J. Laser Appl. 18 (1) (2006) 42–46.

[10] J. Wu, P. Zhao, H. Wei, Q. Lin, Y. Zhang, Development of powder distribution model of discontinuous coaxial powder stream in laser direct metal deposition, Powder Technol. 340 (2018) 449–458.

[11] N. Yang, Concentration model based on movement model of powder flow in coaxial laser cladding, Opt. Laser Technol. 41 (1) (2009) 94–98.

[12] O. Diniz Neto, A. Alcalde, R. Vilar, Interaction of a focused laser beam and a coaxial powder jet in laser surface processing, J. Laser Appl. 19 (2) (2007) 84–88.

[13] A. Mouchard, M. Pomeroy, J. Robinson, B. McAuliffe, S. Donovan, D. Tanner, An analytical method for powder flow characterisation in direct energy deposition, Addit. Manuf. 42 (2021) 101991.

[14] A.J. Pinkerton, Advances in the modeling of laser direct metal deposition, J. Laser Appl. 27 (S1) (2015) S15001.

[15] J. Lin, Numerical simulation of the focused powder streams in coaxial laser cladding, J. Mater Process. Technol. 105 (1–2) (2000) 17–23.

[16] S. Zekovic, R. Dwivedi, R. Kovacevic, Numerical simulation and experimental investigation of gas–powder flow from radially symmetrical nozzles in laser-based direct metal deposition, Int. J. Mach. Tools Manuf. 47 (1) (2007) 112–123.

[17] P. Balu, P. Leggett, R. Kovacevic, Parametric study on a coaxial multi-material powder flow in laser-based powder deposition process, J. Mater Process. Technol. 212 (7) (2012) 1598–1610.

[18] H. Tan, C. Zhang, W. Fan, F. Zhang, X. Lin, J. Chen, W. Huang, Dynamic evolution of powder stream convergence with powder feeding durations in direct energy deposition, Int. J. Mach. Tools Manuf. 157 (2020) 103606.

[19] J. Ibarra-Medina, M. Vogel, A.J. Pinkerton, A cfd model of laser cladding: from deposition head to melt pool dynamics, in: International Congress on Applications of Lasers & Electro-Optics, 2011, Laser Institute of America, 2011, pp. 378–386.

[20] H. Pan, T. Sparks, Y.D. Thakar, F. Liou, The investigation of gravity-driven metal powder flow in coaxial nozzle for laser-aided direct metal deposition process, J. Manuf. Sci. Eng. 128 (2) (2006) 541–553.

[21] S. Liu, Y. Zhang, R. Kovacevic, Numerical simulation and experimental study of powder flow distribution in high power direct diode laser cladding process, Lasers Manuf. Mater. Process. 2 (2015) 199–218.

[22] C. Katinas, W. Shang, Y.C. Shin, J. Chen, Modeling particle spray and capture efficiency for direct laser deposition using a four nozzle powder injection system, J. Manuf. Sci. Eng. 140 (4) (2018).

[23] Q. Chai, X. He, Y. Xing, G. Sun, Numerical study on the collision effect of particles in the gas-powder flow by coaxial nozzles for laser cladding, Opt. Laser Technol. 163 (2023) 109449.

[24] P.A. Cundall, O.D. Strack, A discrete numerical model for granular assemblies, Geotechnique 29 (1) (1979) 47–65.

[25] Y. Guo, J.S. Curtis, Discrete element method simulations for complex granular flows, Annu. Rev. Fluid Mech. 47 (2015) 21–46.

[26] V. Šmilauer, E. Catalano, B. Chareyre, S. Dorofeenko, J. Duriez, A. Gladky, J. Kozicki, C. Modenese, L. Scholtès, L. Sibille, et al., Yade reference documentation, Yade Doc. 474 (1) (2010).

[27] Z. Jardon, P. Guillaume, J. Ertveldt, M. Hinderdael, G. Arroud, Offline powder-gas nozzle jet characterization for coaxial laser-based directed energy deposition, Proc. CIRP 94 (2020) 281–287.

[28] K. Odum, M. Soshi, K. Yamazaki, Measurement and analysis of impact dynamics suitable for modelling pneumatic transport of metallic powder flow through a directed energy deposition nozzle, Adv. Powder Technol. 33 (3) (2022) 103515.

[29] R. Saha, P. Biswas, Temperature and stress evaluation during friction stir welding of inconel 718 alloy using finite element numerical simulation, J. Mater. Eng. Perform. (2021) 1–10.

[30] O.d.O.D. Neto, R.M.C.d.S. Vilar, Interaction between the laser beam and the powder jet in blown powder laser alloying and cladding, in: International Congress on Applications of Lasers & Electro-Optics, 1998, Laser Institute of America, 1998, pp. D180–D188.

[31] O. Diniz Neto, R. Vilar, Physical–computational model to describe the interaction between a laser beam and a powder jet in laser surface processing, J. Laser Appl. 14 (1) (2002) 46–51.

[32] Y. Fu, A. Loredo, B. Martin, A. Vannes, A theoretical model for laser and powder particles interaction during laser cladding, J. Mater. Process. Technol. 128 (1–3) (2002) 106–112.

[33] Y. Huang, M.B. Khamesee, E. Toyserkani, A comprehensive analytical model for laser powder-fed additive manufacturing, Addit. Manuf. 12 (2016) 90–99.

[34] M. Sommerfeld, Modelling of particle–wall collisions in confined gas-particle flows, Int. J. Multiph. Flow 18 (6) (1992) 905–926.